uc3m | Universidad Carlos III de Madrid

e-Archivo

This is a postprint version of the following published document:

Torre, A., Ianiro, A., Discetti, S. & Carlomagno, G. (2018). Evaluation of anisotropic tangential conduction in printed-circuit-board heated-thin-foil heat flux sensors. *International Journal of Heat and Mass Transfer*, vol. 127-A, pp. 1138–1146.

Evaluation of anisotropic tangential conduction in printed-circuit-board heated-thin-foil heat flux sensors

A. F. M. Torre[a,1], A. Ianiro[a,*], S. Discetti[a], G. M. Carlomagno[b]

[a] Universidad Carlos III de Madrid, Aerospace Engineering Research Group, Av. de la Universidad 30, 28911 Leganés, Spain.

[b] Dipartimento di Ingegneria Industriale – Sezione Aerospaziale, University of Naples 'Federico II', Naples 80125, Italy

[*] Corresponding author: aianiro@ing.uc3m.es

[1] Currently in AKKA Technologies, Boulevard Henri Ziegler 7, 31700 Blagnac, France.

Abstract

The effect of the tangential conduction contribution in a thermally anisotropic heated-thin-foil heat flux sensor is examined. A parameter to assess the degree of importance of tangential conduction in the sensor is defined and evaluated in order to justify the need of tangential conduction corrections. Printed circuit boards (PCBs) are typical examples of sensors with anisotropic thermal conduction properties, due to the different conductance values in the directions either parallel or orthogonal to the copper tracks which are placed onto a fiberglass substrate. A parametric study on PCBs with different tracks coverage fraction and copper-to-fiberglass heat conductance ratio is carried out. A revised heated-thin-foil formulation, including a correction for anisotropic thermal properties of the PCB, is experimentally tested. The selected thermo-fluid-dynamic test case is the convective heat transfer of a normally impinging round jet for which axisymmetric maps of the Nusselt number are expected. The anisotropic tangential conduction results in non-axisymmetric temperature distributions. Consequently, if anisotropy is not properly accounted for, non-axisymmetric Nusselt number maps are obtained. The anisotropic conduction effects are shown to be weakly sensitive to the copper tracks coverage fraction while strongly dependent on a parameter called degree of anisotropy, which accounts for the copper-to-fiberglass heat-conductance ratio. Anisotropic conduction effects are found to be almost negligible in PCBs with low values of the degree of anisotropy. Accounting for the anisotropic tangential conduction in the heated-thin-foil formulation allows minimizing the differences between the Nusselt number profiles

measured in the directions parallel and orthogonal to the copper tracks. For all the considered PCBs, differences after correction are found to be below the measurement uncertainty expected for an equivalent thermally-isotropic sensor. The proposed approach also allows reducing below the measurement uncertainty the spread between the Nusselt number values measured with all the considered printed circuit boards, providing measurements practically independent of the sensor characteristics.

Keywords: Convective heat transfer, heat-flux sensors, heated thin foil, printed circuit board.

Nomenclature			
A	reference surface area	q_{in}''	heat flux generated by Joule effect
Bi	Biot number	q_{out}''	heat losses by natural convection
D	nozzle diameter	q_{rad}''	radiation heat flux
H	Nozzle exit to impinging plate distance	x_o	in-plane direction orthogonal to copper tracks
I	current intensity	x_p	in-plane direction parallel to copper tracks
L	characteristic length of the problem	w_c	copper tracks width
Nu	Nusselt number	w_f	copper tracks pitch
Nu_{xo}	Nusselt number profile along the direction *orthogonal* to copper tracks	$\underline{\underline{\Lambda}}$	thermal conductivity tensor
Nu_{xp}	Nusselt number profile along the direction *parallel* to copper tracks	α	degree of anisotropy
Re	Reynolds number based on nozzle exit diameter and bulk velocity	γ^*	copper tracks coverage fraction
T_{amb}	ambient temperature	δ	total foil thickness
T_{aw}	adiabatic wall temperature	δ_c	copper thickness
T_j	jet temperature	δ_f	fiberglass plate thickness
T_{st}	stagnation point temperature	ε	wall emissivity
T_w	wall temperature	θ	copper-to-fiberglass heat conductance ratio
$TCDI$	tangential conduction degree of importance	λ	foil-thermal conductivity coefficient
U	jet bulk velocity at nozzle exit	λ_c	copper thermal conductivity
V	electric voltage	λ_f	fiberglass thermal conductivity
h	convective heat transfer coefficient	λ_o	bulk thermal conductivity orthogonal to the copper tracks direction
h_{out}	natural convection coefficient	λ_p	bulk thermal conductivity parallel to the copper tracks direction
h_{st}	stagnation point convective heat transfer coefficient	μ	dynamic viscosity
k	air thermal conductivity	ρ	density
q_{cond}''	tangential conduction through the foil	ρ_λ	conductivity ratio: λ_o/λ_p
q_{conv}''	heat flux dissipated by convection	σ	Stefan-Boltzmann constant

1. Introduction

The need of thermo-fluid-dynamic efficiency improvement (e.g. in jet engines [1]) or of removing heat from compact spaces [2], is a vigorous driver towards the development of efficient heat transfer enhancement strategies, with consequent strive for advanced and reliable measurement techniques. Measuring heat fluxes in thermo-fluid-dynamics requires both a heat flux sensor (with its related thermo-physical model) and temperature transducers. The most common choice for a fully two-dimensional (2D) non-intrusive temperature transducer is infrared (IR) thermography [3-4]; heat transfer maps can also be obtained using liquid crystals [5] or temperature sensitive paints [6]. These techniques offer the advantage of surface mapping of temperatures, which is a most-needed condition for the analysis of complex 3D flow configurations.

For time-averaged heat transfer investigations (and recently also for unsteady ones, e.g., [7]), a commonly employed sensor is the heated-thin-foil sensor [3-4,8-15] with IR thermography as temperature transducer. State-of-art transducers (with uncertainties below 0.1 K), combined with proper control of the experimental conditions, allow to obtain convective heat transfer maps with relatively low uncertainty, often below 5%. Nonetheless, the directional thermal properties of the heated-thin-foil are often overlooked, thus leading to larger uncertainties if not adequately accounted in the sensor model. In the following, the heated-thin-foil sensor formulation is presented for the general case of anisotropic sensors and the corresponding sources of ambiguity are investigated.

1.1 Heated-thin-foil and anisotropic sensors

The heated-thin-foil sensor [16] provides an evaluation of the convective heat transfer coefficient h based on the energy balance of a thin, uniformly heated foil, which is cooled by the fluid stream flowing on it. As represented in Figure 1, in steady-state conditions, the energy balance of the foil leads to the assessment of the convective heat flux q''_{conv}:

$$q''_{conv} = h(T_w - T_{aw}) = q''_{in} - q''_{rad} - q''_{cond} - q''_{out} \tag{1}$$

The convective heat transfer coefficient h can be evaluated from equation (1) after measuring the wall temperature, both while providing a heat input q''_{in} to the foil (in this case T_w is measured), and under adiabatic flow conditions, i.e. with no heat input (thus measuring the adiabatic wall temperature T_{aw}). The terms q''_{rad} and q''_{cond} are the heat fluxes per unit surface area related to radiation to the ambient and to the tangential conduction through the foil thickness (i.e. along the foil surface), respectively. In case of Direct-Current (DC) Joule heating

and uniform dissipation, $q''_{in} = VI/A$, where V is the voltage applied to the foil contacts, I is the current passing through them and A is the foil surface area. The radiation losses to the ambient are typically evaluated with the Stefan-Boltzmann law $q''_{rad} = \varepsilon\sigma(T_w^4 - T_{amb}^4)$, where T_{amb} is the ambient temperature, σ is the Stefan-Boltzmann constant and ε the emissivity coefficient of the foil surface. The term q''_{out} is typically representative of conduction losses toward an insulating substrate or of natural convection and radiation losses from the foil side non-exposed to the flow, and can be expressed as $h_{out}(T_w - T_{amb})$. This latter term is typically negligible although, when performing experiments with relatively low values of the Nusselt number, it can have a significant impact, e.g. up to 17% of q''_{in} [17]. Within this context, a recent work by Sarkar et al. [18] reports that non-uniformities of the convective heat transfer coefficient (and thus temperature) require local corrections.

The tangential conduction term, inside the energy balance, can represent an important contribution, even greater than 10% of q''_{in} when using steel or constantan foils with a thickness of the order of several tens of microns (see, e.g. [19]), thus a precise estimation of q''_{cond} has to be taken into account in order to reduce measurement uncertainty.
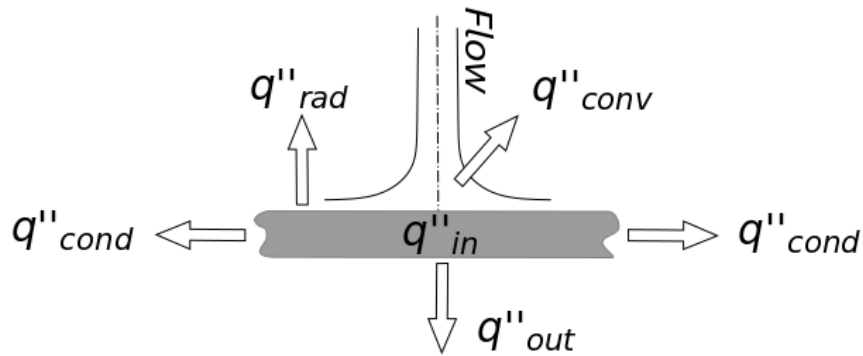

Figure 1 Energy balance of a heated-thin-foil heat flux sensor

If the Biot number $Bi = h\,\delta/\lambda$ (where λ and δ represent the foil thermal conductivity coefficient and thickness, respectively) is relatively small, the foil can be considered isothermal across its thickness. Thus, for isotropic materials and for λ independent of the temperature, from the energy balance in the tangential direction the tangential conduction per unit surface area can be simply evaluated by means of the second derivative of the wall temperature T_w as $q''_{cond} = -\lambda\,\delta\nabla^2 T_w$ [4]. The computation of this derivative is made possible by the high spatial resolution of temperature measurements connected to IR thermography, although it is challenged by the measurement noise, which always requires a careful spatial filtering [20,21].
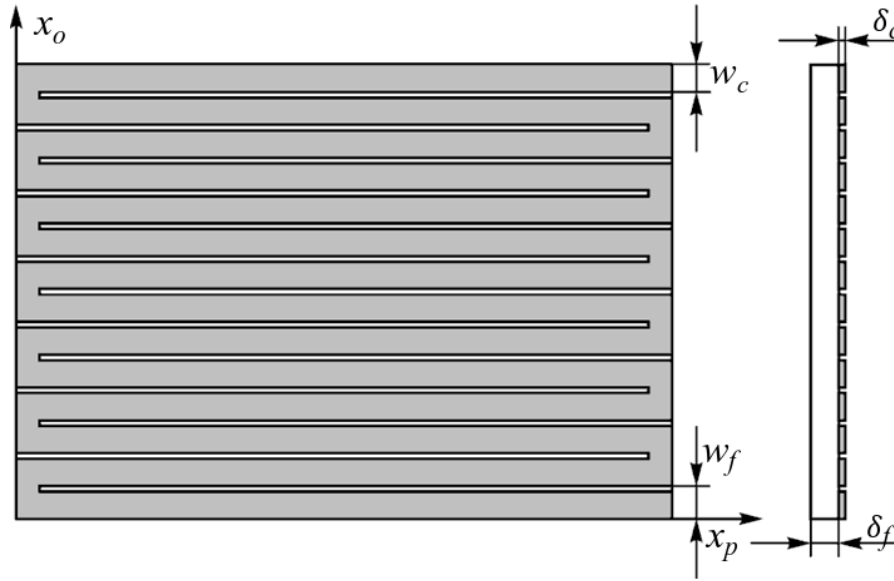
Figure 2 Cartesian axis reference system on the PCB (adapted from [4])

Anyhow, a common experimental choice consists of manufacturing the heated-thin-foil sensor as a printed circuit board (PCB) made of copper tracks bonded on a fiberglass slab. The copper tracks are usually arranged in a Greek fret [10-14] or spiral [9] configuration. The use of a printed circuit board for the design of a spatially uniform heater may be advantageous with respect to a simple foil because it is possible to have a more complex geometry of the heater, such as a non-rectangular one or with the presence of holes inside the heat-exchanging surface [12]. Besides, with a printed circuit board, it is extremely easy to obtain cylindrical or conical geometries (i.e. with a directrix) and electric current intensities are cut down with respect to foils. In order to obtain a spatially uniform distribution of the Joule heating, it is necessary to have a constant copper track cross-section (i.e. width and thickness), a regular arrangement of the tracks and a relatively narrow gap between them. As schematically shown in Figure 2, a simple way to reach this goal is to arrange the tracks in a Greek fret mode with the bends placed at the periphery of the board.

In Figure 2, the copper tracks (in grey) are placed over a fiberglass substrate (in white), have constant width w_c, pitch w_f and thickness δ_c, the fiberglass substrate having a thickness δ_f. The heating of the board is provided passing an electric current through the copper circuit and it can be approximated as spatially uniform if the track gap ($w_f - w_c$) can be considered small as compared to the characteristic length of the tackled thermo-fluid-dynamic problem.

However, the presence of the tracks introduces an anisotropic thermal behaviour of the board. In fact, notwithstanding the copper thinness, the large difference between copper and fiberglass thermal conductivities ($\approx$400W/(mK) versus $\approx$0.25 W/(mK)) results in an

5

anisotropic thermal behaviour of the sensor. As a matter of fact, the value of the bulk thermal conductance in the wall normal direction is practically independent of whether being computed either above a track or a gap since $\lambda_f \ll \lambda_c$ and typically $\delta \approx \delta_f$. Instead, the bulk thermal conductance varies according to if being computed in the direction parallel to the copper tracks (λ_p) or orthogonal to them (λ_o). In this case, the tangential conduction term q_{cond}'' has to be evaluated as:

$$q_{cond}'' = -\delta \underline{\nabla} \cdot \left(\underline{\underline{\Lambda}} \cdot \nabla T_w \right) = -\delta \left(\lambda_o \frac{\partial^2 T_w}{\partial x_o^2} + \lambda_p \frac{\partial^2 T_w}{\partial x_p^2} \right) \tag{2}$$

where $\underline{\underline{\Lambda}}$ is the thermal conductivity tensor, while x_o and x_p are the directions orthogonal and parallel to the copper tracks [22], respectively. Of course, the second equality in equation (2) can be obtained considering bulk properties in the foil.

Following [22] and according to the sketch of Figure 2, the thermal conductance in the x_p direction can be estimated considering that the conductive heat flux along x_p is the sum of two mechanisms in parallel, one due to the copper tracks and the other one to the fiberglass support. Instead along the x_o direction, the conductive heat flux may be ascribed only to fiberglass in the foil zones not covered by the tracks, whereas, in correspondence of the tracks, both materials contribute to conduction; the conductive heat flux can be thus estimated as due to both a series and a parallel processes.

Therefore, the bulk tangential conduction along the direction parallel to the copper tracks can be expressed as:

$$q_{cond,p}'' = -\delta \lambda_p \frac{\partial^2 T}{\partial x_p^2} = -\left(\frac{w_c \delta_c \lambda_c + w_f \delta_f \lambda_f}{w_f} \right) \frac{\partial^2 T}{\partial x_p^2} = -\left(\gamma^* \delta_c \lambda_c + \delta_f \lambda_f \right) \frac{\partial^2 T}{\partial x_p^2} \tag{3}$$

where $\gamma^* = w_c/w_f$ is the copper tracks coverage fraction.

Instead, along the direction orthogonal to the copper tracks, the bulk tangential conduction can be evaluated as:

$$q_{cond,o}'' = -\delta \lambda_o \frac{\partial^2 T}{\partial x_o^2} = -\left[1 / \left(\frac{1-\gamma^*}{\delta_f \lambda_f} + \frac{\gamma^*}{\delta_f \lambda_f + \delta_c \lambda_c} \right) \right] \frac{\partial^2 T}{\partial x_o^2} \tag{4}$$

As evident from equations (3) and (4), the PCB is thermally isotropic only in the limit of $\gamma^* \to 0$, or $\gamma^* \to 1$, as well as for copper-to-fiberglass heat conductance ratio $\theta = \delta_c \lambda_c / \delta_f \lambda_f \ll 1$.

However, since the foil is thermally thin (so its in-plane conductance is relatively small), tangential conduction through the heated-thin-foils might appear negligible if the occurrence of significant local temperature second derivatives is not considered. In fact, it is very frequent to encounter studies in which tangential conduction through the board is neglected or in which the conductance anisotropy is claimed to be negligible (see, eg. [14, 23-25]).

6

Dimensional analysis suggests defining a parameter of Tangential Conduction Degree of Importance $TCDI$ (which matches with the initials of this paper coauthors) as the ratio of the tangential conduction term and the convective one:

$$TCDI = \frac{\lambda \delta \nabla^2 T_w}{h(T_w - T_{aw})} \tag{5}$$

where λ is the isotropic thermal conductivity for an isotropic plate and the maximum one for a thermally anisotropic board. An order of magnitude estimation for the (discrete) second derivative leads to:

$$TCDI = \frac{\lambda \delta (T_{wmax} - T_{wmin})}{h(T_w - T_{aw})L^2} \tag{6}$$

with L being the characteristic lengthscale of the problem. Using eq. (1) and under the assumption that the convective heat flux is the dominant contribution, it follows an operative definition of $TCDI$:

$$TCDI = \frac{\lambda \delta}{Nu_{min} kL} \left(1 - \frac{Nu_{min}}{Nu_{max}}\right) \tag{7}$$

where k is the fluid thermal conductivity and $Nu = hL/k$ is the Nusselt number. The subscripts max and min indicate the maximum and minimum values in the region where the large second derivatives of the convective heat transfer coefficient are expected. For instance, in the case of the classical bell-shaped distribution of heat transfer coefficient for an impinging jet at nozzle-to-plate distance larger than 6 nozzle diameters, the maximum and minimum values can be taken at the stagnation point and at a distance of 1 diameter. According to eq. (7), $TCDI$ can be estimated either *a priori* using literature data or processing raw data without accounting the tangential conduction and using it as an *a posteriori* check.

From the definition of the parameter $TCDI$ it is evident that the $TCDI$ is not just a property of the thin foil but strongly depends on the thermo-fluid-dynamic problem under consideration and can easily account for a significant percentage of h if the problem characteristic length is small enough and Nu variations are large enough.

The objective of the present study is to analyse the effects of tangential conduction in heated-thin-foil heat flux sensors made of a printed circuit board and to quantify the accuracy of the tangential conduction evaluation provided by equations (3) and (4). Convective heat transfer measurements are performed on a round impinging jet [26] by using printed circuit board sensors with different geometries, allowing to assess the effect of γ^* and θ. The axial symmetry of the experimental configuration offers a straightforward detection of anisotropy effects of the sensors. The measurements corrected making use of equations (3) and (4) are compared with respect to those obtained considering isotropic conduction or neglecting

tangential conduction through the foil; this is to demonstrate that equations (3) and (4) provide finer results and allow for a minimization of the experimental uncertainty.

2 Experimental apparatus and data analysis approach

2.1 Experimental apparatus and details

The experiments are carried out in the impinging jet facility (sketched in Figure 3) of the Aerospace Engineering Laboratories of the Universidad Carlos III de Madrid.
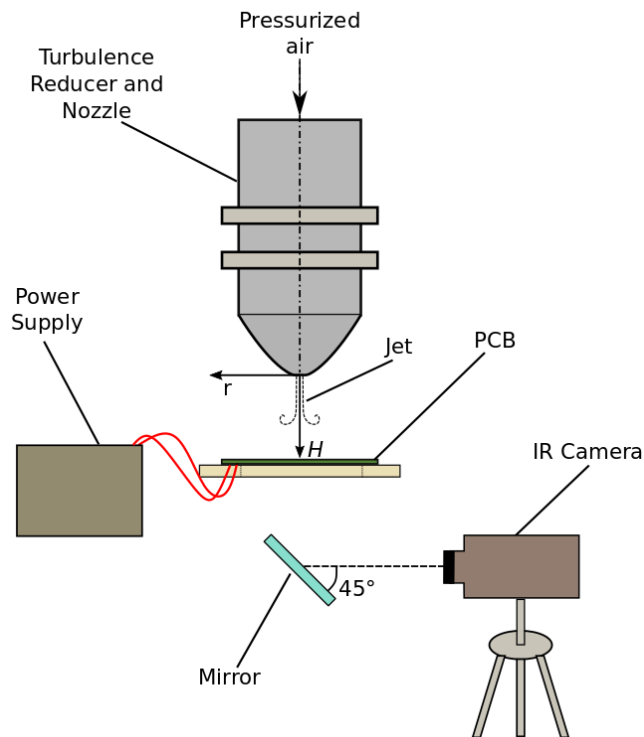

Figure 3 Sketch of the impinging jet facility and of the experimental setup for heated-thin-foil measurements with IR thermography

A constant and stable air mass flow rate is provided to a stagnation chamber, where the stagnation conditions are monitored. The chamber is equipped with honeycomb flow straighteners and screens to reduce the free stream turbulence.

The jet issues from a contoured, bell-shaped convergent nozzle, with an exit diameter $D = 20mm$, resulting in a bulk Reynolds number $Re = \rho UD/\mu = 20 \cdot 10^3$, where ρ and U are the fluid density and the jet bulk velocity at nozzle exit, respectively. Since the phenomenon under study depends on the temperature second spatial derivatives, certainly the selected D value is relatively large, but it was decided to choose it to macroscopically neglect the highest gap value between the tracks $w_f - w_c = 1mm$ (see Table 1). The jet exit bulk velocity U is

estimated from the difference between stagnation (in the chamber) and static pressure (at the nozzle exit) with a differential pressure transducer having an uncertainty of 1 Pa. The contoured nozzle ensures a uniform velocity profile at the exit [27], enabling negligible pressure losses. Being the jet Mach number at nozzle exit very low and $T_j \approx T_{amb}$, it is $T_{aw} \approx T_j$.

The accelerated jet flow orthogonally impinges on the printed-circuit-board sensor. The temperature distribution on the board is imaged with an IR camera from the side opposite to impingement. This side is coated with a thin layer of opaque-black enamel that allows high emissivity coefficient, thus enhancing the accuracy of the IR temperature measurements. Actually, the IR camera images a 45° inclined first-surface mirror located at approximately $30cm$ from both the rear side of the PCB and the camera. Care is taken to ensure orthogonal imaging of the surface in order to guarantee uniform magnification. IR camera recorded signal is carefully calibrated with a black body, ensuring a temperature measurement uncertainty below $0.1K$.

A DC stabilized power supply provides a constant current to the printed circuit board. This source guarantees a reliable and stable current with the precision of $10^{-2}A$. The power setting is chosen in order to obtain the minimum temperature difference between power on and power off conditions not less than about $5K$ in all the experiments. The PCB is screwed at its outer edge to a methacrylate frame. Using empirical correlations of a heated plate facing downward [28], natural convection losses are estimated to account for less than 1% of q''_{in}. Image noise is reduced acquiring ensemble averaging a total of 2000 images, for both the "hot" (with electric power supplied to the circuit) and "cold" (with power off) images.

The nozzle-to-plate distance H is varied by moving the nozzle along the axial direction and experiments are performed for H equal to either two or six nozzle diameters.

A total of 6 different printed circuit boards, each with an area of $210 \times 210 \ mm^2$ and whose characteristics are reported in Table 1, are tested. The selected PCBs have different values of w_c, w_f (thus different values of the gap between copper tracks), δ_c, θ, and γ^*; instead, the fiberglass substrate thickness is kept at a constant value equal to 0.5 mm. The adopted circuit nomenclature is WxGyDz, where x indicates the track pitch w_f in mm, y is the gap $(w_f - w_c)$ in tenths of mm and z is the copper layer thickness δ_c in μm.

PCB NAME	w_c (mm)	w_f (mm)	gap (mm)	δ_c (μm)	δ_f (mm)	γ^*	θ
W2G10D15	1	2	1	15	0.5	0.5	48
W2G02D15	1.8	2	0.2	15	0.5	0.90	48
W2G02D30	1.8	2	0.2	30	0.5	0.90	93.8
W2G02D05	1.8	2	0.2	5	0.5	0.90	12.8
W2G04D15	1.6	2	0.4	15	0.5	0.80	48
W4G04D15	3.6	4	0.4	15	0.5	0.90	48

Table 1 PCB parameters

For each circuit, it is possible to obtain the two bulk conductivities in the direction orthogonal λ_o and parallel λ_p to the copper tracks and their ratio $\rho_\lambda = \lambda_o/\lambda_p$, as well as to assess the *degree of anisotropy* $\alpha = (\lambda_p/\lambda_o - 1)$ of each board to rank them as in Table 2. In the table, $TCDI$ is evaluated for $H/D = 2$ by considering the typical values of the Nusselt number at the stagnation point Nu_{max} (of the order of 125) and at the characteristic length distance of one nozzle diameter ($Nu_{min} \approx 95$). For the calculation of $TCDI$ a value of the thermal conductivity of air $k = 0.025\,W/mK$ has been used. It is interesting to notice that the circuits W2G10D15 and W2G02D30 have the larger degree of anisotropy which might suggest higher measurement errors; however, the values of $TCDI$ suggests greater errors for W2G02D30. Of course, for smaller nozzle diameters, $TCDI$ would be higher.

PCB	λ_p [$W/(m \cdot K)$]	λ_o [$W/(m \cdot K)$]	ρ_λ	$(\lambda_p - \lambda_o)/\lambda_0$	$TCDI$ $\dfrac{\lambda\delta}{Nu_{min}kL}\left(1 - \dfrac{Nu_{min}}{Nu_{max}}\right)$
W2G10D15	6.3	0.5	0.08	10.9	16‰
W2G02D30	21.2	2.3	0.11	8.3	54‰
W2G04D15	9.9	1.2	0.13	7.0	25‰
W4G04D15	11.3	2.2	0.20	4.1	29‰
W2G02D15	11.1	2.2	0.20	4.0	28‰
W2G02D05	3.1	1.6	0.5	1.0	8‰

Table 2 Equivalent conductivity in the directions x_o and x_p, their ratio $\rho_\lambda = \lambda_o/\lambda_p$, degree of anisotropy and $TCDI$ of the PCBs.

2.2 Data analysis approach

Experimental measurements of the convective heat transfer coefficient are reduced in non-dimensional form in terms of both temperature difference maps and conventional Nusselt number $Nu = hD/k$ profiles. The Nu results obtained by evaluating tangential conduction with eqs. (3) and (4) are compared with respect to two simplified modes:

- isotropic tangential conduction approximation (the tangential conduction term is estimated as $-\lambda \, \delta \nabla^2 \, T_w$, considering an isotropic thermal conductance equal to the average of the thermal conductances along the directions orthogonal and parallel to the copper tracks);
- neglecting in eq. (1) the tangential conduction term.

The evaluation of the Nusselt number uncertainty follows the method described by Moffat [29] and considers, for all the measured parameters, the measurement uncertainties reported in Table 3. The Nusselt number uncertainty is estimated to be lower than 3%.

Parameter	Uncertainty	Typical value
$T_w - T_{aw}$	2%	$> 5 \, [K]$
$T_w - T_{amb}$	2%	$> 5 \, [K]$
V	0.20%	$30 \, [V]$
I	0.20%	$3 \, [A]$
k	1%	$0.0265 \, [W/(m{*}K)]$
ε	1%	0.95
A	0.10%	$0.0441 \, [m^2]$
δ	0.10%	$0.0005 \, [m]$
d^2T/dx^2	10%	$-1.42 \, [K/m^2]$
λ	1%	$0.25 \, [W/(m{*}K)]$
D	0.10%	$0.02 \, [m]$

Table 3 Uncertainty analysis

3 Results

Depending on the nozzle-to-plate distance H, Nusselt number distributions of round impinging jets can be either bell shaped with a maximum on the jet axis (if the nozzle-to-plate

distance is sufficiently large) or can exhibit a number of annular regions of local Nu maxima (if the jet impinges within its potential core, i.e. $H/D < 4$) [26].

Convective heat transfer measurements have been performed at two nozzle-to-plate distances, namely $H/D = 2$ and 6.

The case at $H/D = 2$ allows to compare the measurement of Nu profiles in the x_p and x_o directions due to the presence of multiple local maxima-minima of Nu. The different values of the conductance along these two directions result in different temperature profiles and non-axisymmetric distributions of the temperature maps.

The bell-shaped Nusselt number distribution experienced by the configuration at $H/D = 6$ results in very strong tangential conduction effects nearby the jet stagnation point, corresponding to the location of the Nusselt number maximum. Therefore, stagnation point Nusselt number measurements at $H/D = 6$ are used to assess the capability of the correction provided by eqs. (3) and (4) to reduce the data spread amongst the results obtained with the different PCBs.

3.1 Quantification of conduction effects

The configuration of the impinging jet with $H/D = 2$ is particularly interesting since the Nusselt number maps are characterized by two local maxima (and minima) [26], in correspondence of which large absolute values of temperature second derivatives (and thus tangential conduction heat flux) occur. This results in significant differences between the temperature profiles measured along the x_o and x_p directions. For the six considered printed circuit boards, Figure 4 reports the temperature difference distributions $T_w - T_{aw}$, normalized with respect to the difference between the temperature at the stagnation point T_{st} with Joule heating and the jet temperature T_j measured over the non-heated-thin-foil, while impinged by a round jet at $H/D = 2$. For most of the boards, the conductance anisotropy determines an elliptical shape of the temperature contours, with major axis along the x_p direction. Indeed, for radial distances higher than half diameter from the stagnation point, the thermal distribution loses its axial symmetry, especially for a high degree of anisotropy α.

For explanatory purposes, under the same conditions reported in Figure 4, Figure 5 visualizes the maps of the absolute contribution to the Nusselt number due to conduction heat fluxes within the sensor owing to anisotropy, for the two boards W2G02D30 and W2G02D05, which differ only for the copper track thickness and are characterized by $TCDI$ values of 54‰ and

12

8‰. In these maps, also the Nusselt number contours are shown and the degree of anisotropy α is indicated in the caption.

The thicker copper tracks of W2G02D30, characterized by a large degree of anisotropy $\alpha = 8.3$ and a relevant value of $TCDI$, result in strong conduction contributions to the Nusselt number, mainly along the x_p direction. The values of the maximum positive and the minimum negative contribution to the Nusselt number are in line with the 54‰ level of the parameter $TCDI$. On the contrary W2G02D05, which has lower $\alpha = 1.0$ and $TCDI = 8$‰, besides showing much lower contributions to Nu, exhibits a more isotropic tangential conduction (indeed the board has the lowest δ_c), which means a rather similar magnitude of the conduction heat flux in the x_o and x_p directions. In this case, $TCDI$ provides a good estimation of the difference between the maximum positive and minimum negative contribution to the Nusselt number.
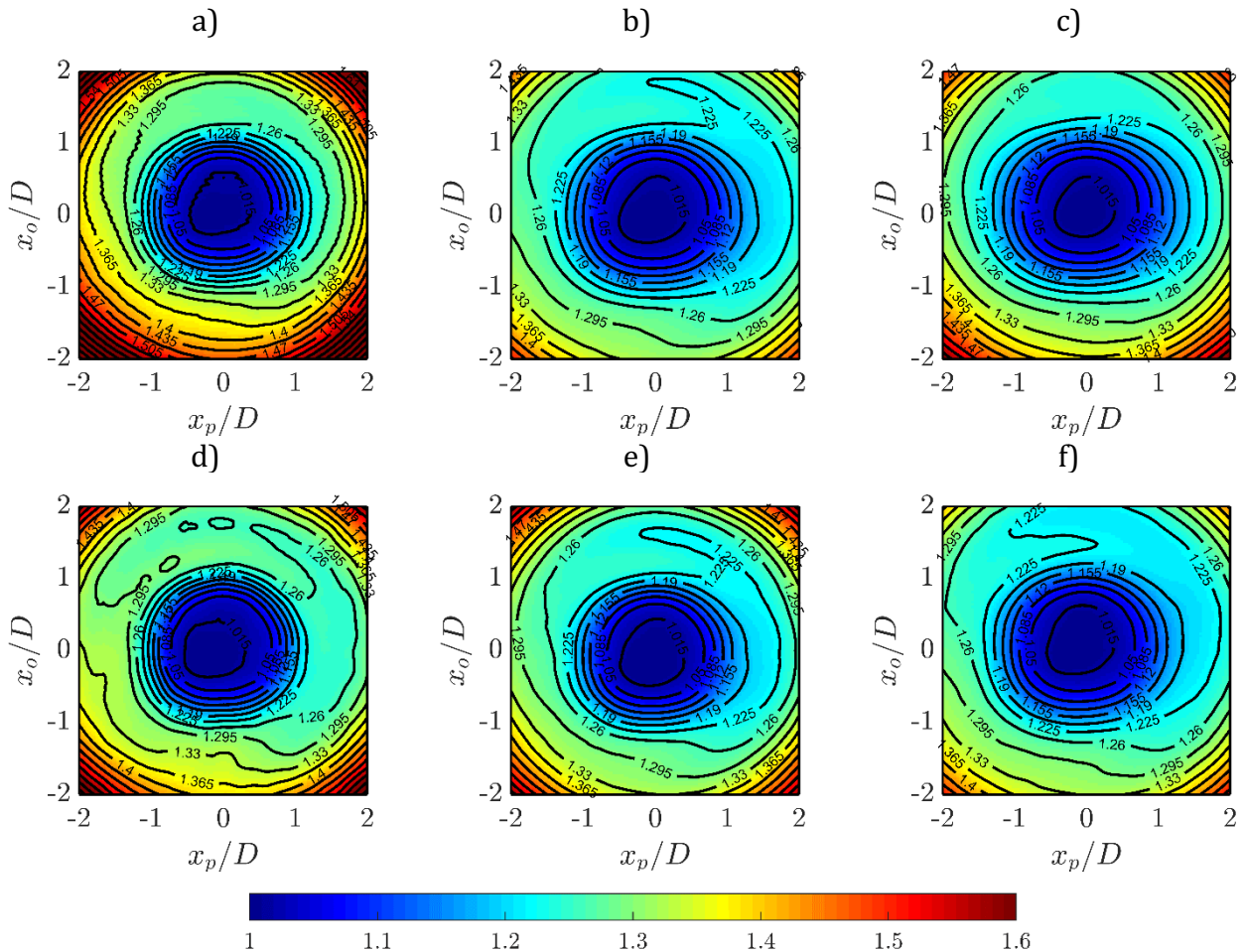

Figure 4 Non-dimensional foil temperature difference maps $(T_w - T_{aw})/(T_{st} - T_j)$ measured for nozzle to plate distance equal to 2 diameters. W2G10D15, $\alpha = 10.9$ (a), W2G02D15, $\alpha = 4.0$ (b), W2G02D30, $\alpha = 8.3$ (c), W2G02D05, $\alpha = 1.0$ (d), W2G04D15, $\alpha = 7.0$ (e), W4G04D15, $\alpha = 4.1$ (f).
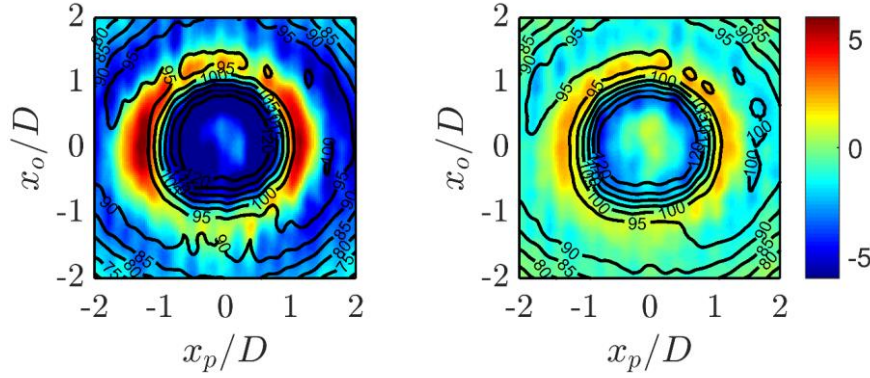
Figure 5 Contour plots of the Nusselt number contribution due to conduction heat fluxes generated within the sensor due to anisotropy. W2G02D30, $\alpha = 8.3$, $TCDI = 54‰$ (Left) and W2G02D05, $\alpha = 1.0$, $TCDI = 8‰$ (Right).

Figure 6 reports a comparison between the Nusselt number radial profiles along the x_o and x_p directions evaluated by correcting the tangential conduction as in eqs. (3) and (4) (solid lines, anisotropic correction) and the two simplified models of either isotropic correction (dashed lines) or ignored conduction (dotted lines). The x_o Nu profile obtained for the circuit W2G02D05 with anisotropic tangential conduction is considered as a reference value. The shadowed regions cover the 3% deviation from the reference profile, which corresponds to the maximum Nusselt number uncertainty.

For all the PCBs, the anisotropic correction allows reducing the difference between the values of the Nusselt number at a given radial position along the x_o and x_p directions. The use of this correction also allows to obtain a measured Nusselt number profile which, within the measurement uncertainty, is practically independent of the sensor characteristics. The effects of the correction are more appreciable (Figure 6 a-c) for sensors having larger degree of anisotropy α, e.g., W2G02D30 ($\alpha = 10.9$) and W2G02D15 ($\alpha = 8.3$). In these two cases a large error is introduced when the isotropic correction is applied. A discrepancy of up to the 13% of the stagnation-point Nusselt number between the two profiles is visualized (W2G02D30, Figure 6c). This leads to an effective uncertainty which is well above the one estimated with Table 3. Considering the anisotropic correction, the differences between Nu profiles in the x_p and x_o directions is reduced to less than 3% of the stagnation point Nu for all the tested PCBs.

The profiles corresponding to W2G02D05 are characterized by the minimum discrepancy among the set of PCBs; this is because α in this case is minimum ($\alpha = 1$). Nonetheless, the correction for anisotropy is still found effective to achieve further reduction of the

inconsistencies between the profiles, especially nearby the outer local Nu maximum located at $r/D \approx 1.7$, which is barely visible if the tangential conduction term is ignored. It should be remarked the case of W2G10D15 ($\alpha = 10.9$), which still allows for quite precise corrected results despite the large gap between the copper tracks. In this case, the gap equal to 5% of the problem characteristic length D seems not to introduce very relevant errors.
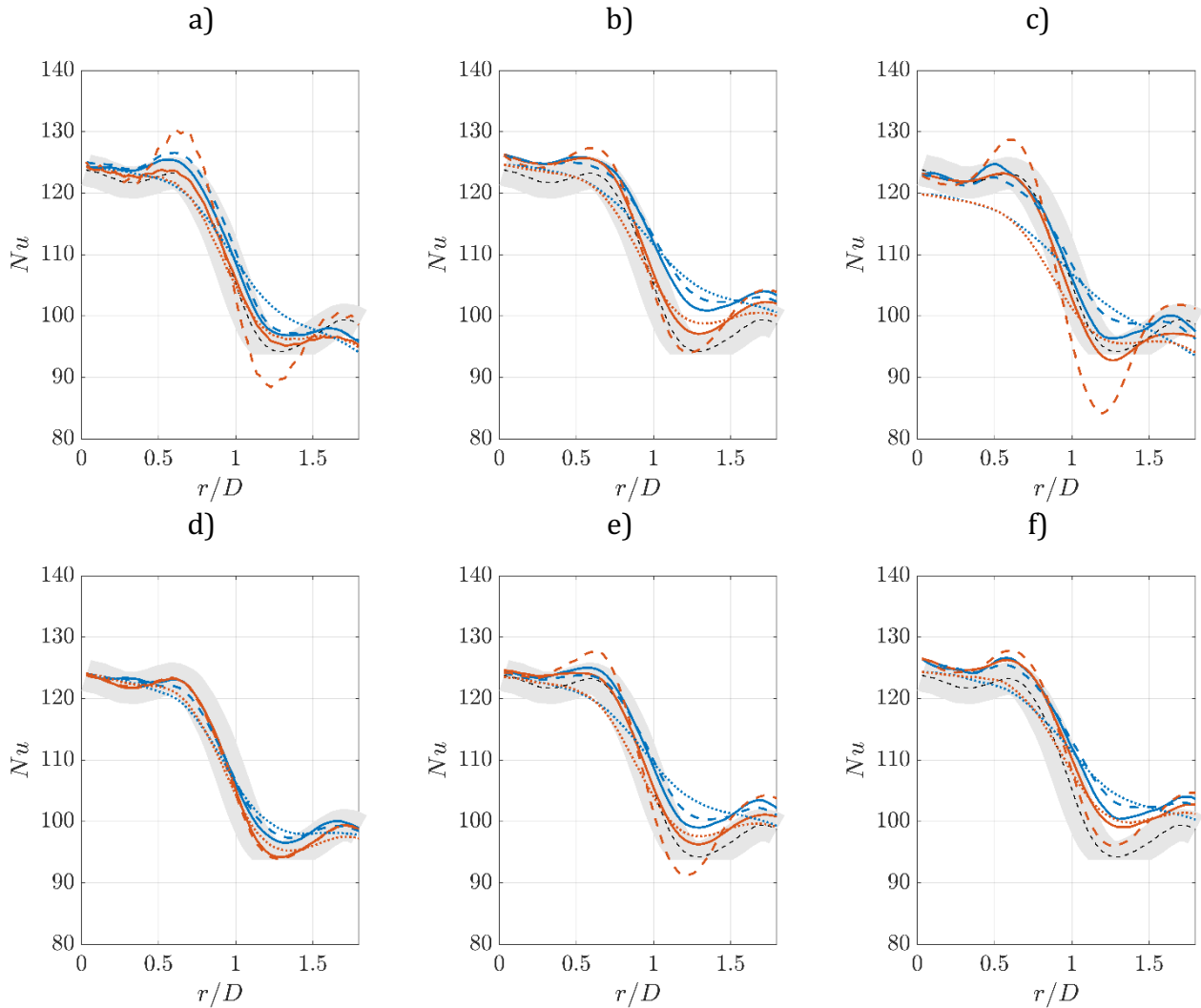

Figure 6 $x_p -$ (blue) and $x_o -$ (red). Nu profiles comparisons for H/D = 2. W2G10D15, $\alpha = 10.9$ (a), W2G02D15, $\alpha = 7.0$ (b), W2G02D30, $\alpha = 8.3$ (c), W2G02D05, $\alpha = 1.0$ (d), W2G04D15, $\alpha = 4.1$ (e), W4G04D15, $\alpha = 4.1$ (f). Continuous lines represent the anisotropic conductivity corrected, dashed lines considering an isotropic tangential conduction and dotted lines the results neglecting tangential conduction. The $x_o -$ (black) Nu profile obtained for W2G02D05 is considered as a reference value. Dashed regions cover the 3% deviation profile. from the reference value.

3.2 Effect of the copper tracks gap: γ*

In order to ascertain the effect of the tracks gap on the tangential conduction through the printed circuit boards, this section reports a comparison between the sensors W2G10D15,

W2G04D15 and W2G02D15 (i.e. at fixed copper and fiberglass thickness, resulting in copper-to-fiberglass heat conductance ratio $\theta = 48$). These sensors have the same copper tracks pitch w_f and thickness δ_c, while differ only for the copper tracks width, w_c, i.e. the gap $(w_f - w_c)$ between the tracks (see Table 1). These circuits are characterized by $\gamma^* = w_c/w_f$ respectively equal to 0.5, 0.8 and 0.9. The parameter γ^* quantifies the coverage of the copper tracks layer above the plate. The difference between the Nusselt number radial profiles measured in the x_o and x_p directions, normalized with the stagnation point Nusselt number, is reported in Figure 7. In particular, Figure 7a shows the result obtained neglecting the tangential conduction term. The maximum deviation among the two profiles is found in correspondence of the local Nu minimum located at $r/D \approx 1.2$. The effect of γ^* is practically negligible and the three curves almost collapse below measurement uncertainty. The differences between the Nu profiles in the x_o and x_p directions and the loss of axial symmetry are further stressed when including the tangential conduction using the isotropic model (Figure 7b). Indeed, in this case the conduction term is underestimated along the tracks direction and is overestimated along the direction orthogonal to the tracks. This effect is more intense for small γ^*, thus the error increase for W2G10D15 is maximum.

If the anisotropic tangential conduction model is used for the three tested sensors, the difference between the Nu profiles along the x_o and x_p directions drops below the measurement uncertainty, thus showing that the methodology proposed by eqs. (3) and (4) is able to reduce tangential conduction non-uniformity effects in a wide range of γ^* values.
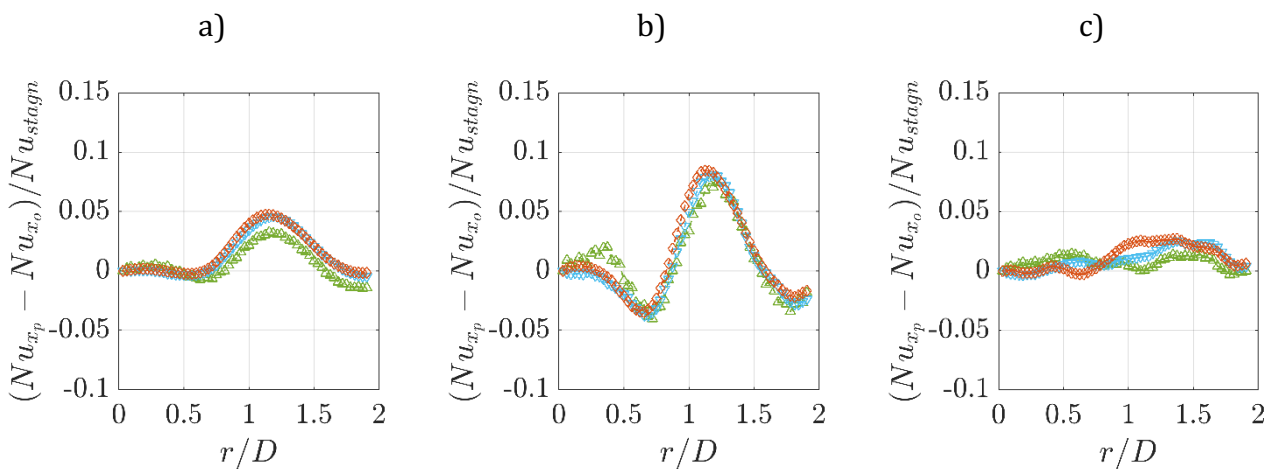

Figure 7 Effect of γ^* on the Nu profiles. ◊- W2G02D15 ($\gamma^* = 0.9$); ▽- W2G04D15 ($\gamma^* = 0.8$); △- W2G10D15 ($\gamma^* = 0.5$). (a) neglecting tangential conduction; (b) isotropic tangential conduction; (c) anisotropic tangential conduction

3.3 Effect of copper-to-fiberglass heat conductance ratio θ

The effect of the copper-to-fiberglass heat conductance ratio (copper tracks thickness) can be assessed by comparing the Nusselt number profiles measured with the sensors W2G02D05 ($\theta = 12.8, \alpha = 1$), W2G02D15 ($\theta = 48.0, \alpha = 4.0$) and W2G02D30 ($\theta = 93.8, \alpha = 8.3$) which are all characterized by the same value of $\gamma^* = 0.90$. This effect is shown in Figure 8.

For smaller values of θ, the conduction through the copper is stronger and larger differences between the x_o and x_p profiles are expected. When neglecting the tangential conduction, the profiles in the x_o and x_p directions measured with the W2G02D15 sensor present differences of about 2% of the stagnation point Nusselt number, the W2G02D30 results in greater differences of about 3% while the W2G02D05 shows differences below 0.5%. These differences are increased when considering isotropic conduction; nonetheless very good results are obtained for the sensor W2G02D05 due to both the small value of θ and the high value γ^*. All the results are improved when employing anisotropic tangential conduction correction (Figure 8 c).

3.4 Reduction of uncertainty

Table 4 reports the absolute values of the Nusselt number measured at the stagnation point for the case of $H/D = 6$. The results are estimated by either neglecting tangential conduction, or considering isotropic conduction through the printed circuit board or else using the correction of eqs. (3) and (4). Neglecting tangential conduction effects results in a significant data spread, with a systematic underestimation of Nu at the stagnation point for larger values of the conductance. In fact, the spread, reported in the last row of the table, is of almost 6.5% of the mean of all the measured values when neglecting the tangential conduction term. The spread remains practically unaltered (6.9%) if tangential conduction losses are estimated with an isotropic model. By taking into account the anisotropic conduction by means of equations (3)-(4), the data spread is reduced to 3.1% -thus about the measurement uncertainty– which seems to achieve the best measurement precision.
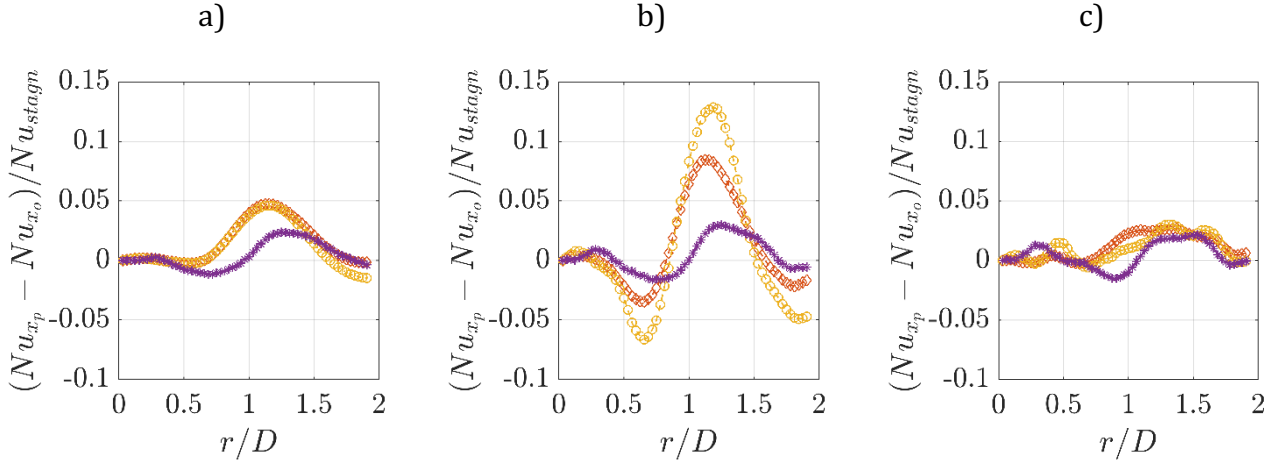
Figure 8: Effect of θ on the Nu profiles. $*$- W2G02D05 ($\theta = 12.8, \alpha = 1$); ◊- W2G02D15 ($\theta = 48.0, \alpha = 4.0$); ○- W2G02D30 ($\theta = 93.8, \alpha = 8.3$). (a) neglecting tangential conduction; (b) isotropic tangential conduction; (c) anisotropic tangential conduction.

Board	Neglected conduction	Isotropic conduction	Anisotropic conduction
W2G10D15	127	135	131
W2G02D15	125	132	131
W2G02D30	121	132	130
W2G02D05	125	127	127
W2G04D15	125	132	130
W4G04D15	119	126	128
Mean	123.7	130.7	129.5
MAX	127	135	131
min	119	126	127
Spread %	6.5	6.9	3.1

Table 4 Stagnation point Nusselt number values measured for $H/D = 6$: neglecting tangential conduction, accounting for isotropic conduction and for anisotropic conduction. The spread is computed as $(MAX - min)/Mean$.

4 Conclusions

The effect of the thermal conduction properties of PCB sensors, used for the heated-thin-foil implementation in convective heat transfer measurements, has been analysed. A parameter to assess the importance of the tangential conduction losses has been defined and assessed as $TCDI = \frac{\lambda \delta}{Nu_{min} kL}\left(1 - \frac{Nu_{min}}{Nu_{max}}\right)$, taking into account the foil thermal conductivity and thickness and the problem characteristic convective heat transfer coefficient and length. This aspect is of particular importance when using printed circuit boards, whose anisotropy might significantly affect the measured Nusselt number distributions. In fact, it has been demonstrated that, if the tangential conduction is neglected or improperly modelled (e.g.,

using an isotropic model), the measurements can be jeopardized, leading to larger measurement uncertainty. A formulation including anisotropic conductance is tested using a round impinging jet configuration, in which the axial-symmetry of the problem is a good check for distortion effects due to anisotropic thermal properties of the sensor. Six different track geometries of the PCBs have been tested to assess the effects on the measurement uncertainty and a degree of anisotropy α has been defined. The formulation with anisotropic thermal properties correction reduces the differences between Nu profiles in the track-parallel and track-normal directions to less than 3%, while larger deviations were displayed when an isotropic in-plane conduction model was adopted for the calculations. The differences found in these cases reach values up to 10%. It should be remarked that for a printed circuit board with a gap between copper tracks equal to 5% of the problem characteristic length, the correction allows for quite precise results.

For the case of nozzle-to-plate distance equal to 6 diameters, in which a bell-shaped distribution of the Nusselt number is expected, the formulation with anisotropic correction has demonstrated to provide consistent results independently of the selected PCB. In this case, the final data spread is about the measurement uncertainty (3%). A much larger data spread is instead observed for the case of either isotropic conduction model or if the tangential conduction is neglected.

The results herein presented indicate that, for small values of the degree of anisotropy α and/or for small values of $TCDI$, accounting for anisotropic conduction is not strictly required. Indeed, for the board W2G02D05 (having the lowest $\alpha = 1$ and $TCDI = 8‰$) the results reported in Table 4 show good agreement independently on the use of an isotropic or an anisotropic conduction model.

Since the studied phenomenon depends on the temperature second spatial derivatives, according to the definition of $TCDI$, the choice of a smaller D value would have further increased the tangential conduction influence.

Acknowledgments

References

[1] Han, J. C., Dutta, S., & Ekkad, S. (2012). Gas turbine heat transfer and cooling technology. CRC Press.

[2] Garimella, S. V., Yeh, L. T., & Persoons, T. (2012). Thermal management challenges in telecommunication systems and data centers. IEEE Transactions on Components, Packaging and Manufacturing Technology, 2, 1307-1316.

[3] Carlomagno, G. M., & Cardone, G. (2010). Infrared thermography for convective heat transfer measurements. Experiments in fluids, 49, 1187-1218.

[4] Astarita, T., & Carlomagno, G. M. (2012). Infrared thermography for thermo-fluid-dynamics. Springer Science & Business Media.

[5] Ireland, P. T., & Jones, T. V. (2000). Liquid crystal measurements of heat transfer and surface shear stress. Measurement Science and Technology, 11, 969.

[6] Liu, T., & Sullivan, J. P. (2006). Pressure and Temperature Sensitive Paints. Springer Science & Business Media.

[7] Raiola, M., Greco, C. S., Contino, M., Discetti, S., & Ianiro, A. (2017). Towards enabling time-resolved measurements of turbulent convective heat transfer maps with IR thermography and a heated thin foil. International Journal of Heat and Mass Transfer, 108, 199-209.

[8] De Luca, L., Guglieri, G., Cardone, G., & Carlomagno, G. M. (1995). Experimental analysis of surface flow on a delta wing by infrared thermography. AIAA journal, 33, 1510-1512.

[9] Cardone, G., Astarita, T., & Carlomagno, G. M. (1997). Heat transfer measurements on a rotating disk. International Journal of Rotating Machinery, 3, 1-9.

[10] Buchlin, J. M. (2002). Convective heat transfer in a channel with perforated ribs. International journal of thermal sciences, 41, 332-340.

[11] Fénot, M., Vullierme, J. J., & Dorignac, E. (2005). Local heat transfer due to several configurations of circular air jets impinging on a flat plate with and without semi-confinement. International journal of thermal sciences, 44, 665-675.

[12] Giordano, R., Ianiro, A., Astarita, T., & Carlomagno, G. M. (2012). Flow field and heat transfer on the base surface of a finite circular cylinder in crossflow. Applied Thermal Engineering, 49, 79-88.

[13] He, C., Liu, Y., Peng, D., & Yavuzkurt, S. (2016). Measurement of flow structures and heat transfer behind a wall-proximity square rib using TSP, PIV and split-fiber film. Experiments in Fluids, 57(11), 165.

[14] Mallor, F., Vila, C. S., Ianiro, A., & Discetti, S. (2018). Wall-mounted perforated cubes in a boundary layer: Local heat transfer enhancement and control. International Journal of Heat and Mass Transfer, 117, 498-507.

[15] Cafiero, G., Discetti, S., & Astarita, T. (2014). Heat transfer enhancement of impinging jets with fractal-generated turbulence. International Journal of Heat and Mass Transfer, 75, 173-183.

[16] Carlomagno G.M, de Luca l., Cardone G., & Astarita T. (2014). Heat Flux Sensors for Infrared Thermography in Convective Heat Transfer. Sensors, 14, 21065-21116

[17] Greco, C. S., Paolillo, G., Ianiro, A., Cardone, G., & de Luca, L. (2018). Effects of the stroke length and nozzle-to-plate distance on synthetic jet impingement heat transfer. International Journal of Heat and Mass Transfer, 117, 1019-1031.

[18]   Sarkar, D., Jain, A., Goldstein, R. J., & Srinivasan, V. (2016). Corrections for lateral conduction error in steady state heat transfer measurements. International Journal of Thermal Sciences, 109, 413-423.

[19]   Ianiro, A., & Cardone, G. (2012). Heat transfer rate and uniformity in multichannel swirling impinging jets. Applied Thermal Engineering, 49, 89-98.

[20]   Rainieri, S., Bozzoli, F., & Pagliarini, G. (2004). Wiener filtering technique applied to thermographic data reduction intended for the estimation of plate fins performance. Experimental Thermal and Fluid Science, 28, 179-183.

[21]   Carlomagno, G. M., Discetti, S., & Astarita, T. (2011). Experimental assessment of a new heat flux sensor for measuring convective heat transfer coefficients. Quantitative InfraRed Thermography Journal, 8, 37-49.

[22]   Astarita, T., & Cardone, G. (2000). Thermofluidynamic analysis of the flow in a sharp 180 turn channel. Experimental Thermal and Fluid Science, 20, 188-200.

[23]   Fenot, M., Dorignac, E., & Vullierme, J. J. (2008). An experimental study on hot round jets impinging a concave surface. International Journal of Heat and Fluid Flow, 29, 945-956.

[24]   Fénot, M., Dorignac, E., & Lalizel, G. (2015). Heat transfer and flow structure of a multichannel impinging jet. International Journal of Thermal Sciences, 90, 323-338.

[25]   Geng, L., Zheng, C., & Zhou, J. (2015). Heat transfer characteristics of impinging jets: The influence of unsteadiness with different waveforms. International Communications in Heat and Mass Transfer, 66, 105-113.

[26]   Carlomagno, G. M., & Ianiro, A. (2014). Thermo-fluid-dynamics of submerged jets impinging at short nozzle-to-plate distance: A review. Experimental thermal and fluid science, 58, 15-35.

[27]   Violato, D., & Scarano, F. (2011). Three-dimensional evolution of flow structures in transitional circular and chevron jets. Physics of Fluids, 23, 124104.

[28]   Wong, H. Y. (1977). Handbook of essential formulae and data on heat transfer for engineers. Addison-Wesley Longman Ltd.

[29]   Moffat, R. J. (1988). Describing the uncertainties in experimental results. Experimental thermal and fluid science, 1, 3-17.